Contents lists available at ScienceDirect

Applied Catalysis B: Environmental

Physicochemical properties of WO_x/ZrO_2 catalysts for palmitic acid esterification

Vannia Cristina dos Santos [a], Karen Wilson [b], Adam. F. Lee [b], Shirley Nakagaki [a],*

[a] Laboratório de Química Bioinorgânica e Catálise, Universidade Federal do Paraná (UFPR), CP 19081, CEP 81531-990, Curitiba, Paraná, Brazil
[b] European Bioenergy Research Institute, Aston University, Aston Triangle, Birmingham B4 7ET, UK

ARTICLE INFO

ABSTRACT

A series of WO_x/ZrO_2 with various tungsten loadings was prepared via incipient-wetness impregnation of zirconium hydroxide. The resulting thermally processed materials were characterised by XRD, XPS, porosimetry, NH_3-TPD and pyridine FTIR spectroscopy to elucidate their composition, morphology and acidity, and subsequently tested in the esterification of palmitic acid with methanol. Catalytic performance was strongly dependent upon calcination temperature and W surface density. Esterification activity increased with increasing surface W density, reaching a maximum at 8.9 W nm^{-2} corresponding to near monolayer coverage. Subsequent growth of crystalline WO_3 lowered activity, consistent with a decrease in the density of active surface sites. Calcination temperatures as high as 800 °C increased surface acidity and hence catalytic activity. The formation of polymeric tungstate species on zirconia is necessary to generate the Brönsted acid sites responsible for palmitic acid esterification under mild conditions.

© 2014 Elsevier B.V. All rights reserved.

1. Introduction

Catalysis is a key technology by which to deliver sustainable (green) chemistry. Metal oxides are widely employed as heterogeneous catalysts for application in the petrochemical, fine chemical and pharmaceutical sectors, and for environmental remediation [1–4]. The nature of the active catalytic species in such inorganic oxide materials, and particularly mixed metal oxides wherein the interfacial interaction between each component imparts a novel synergy, has received much attention because it affords the means by which to predict and control reactivity. In this respect, the strong acidity of zirconia-supported metal sulfates affords low cost catalysts well-suited to important reaction classes such as alkylation and isomerisation [5–7].

Tungstated zirconia (WO_x/ZrO_2) is a prototypical mixed oxide solid acid catalyst, exhibiting higher acidity and stability than sulfated zirconia. Structure–activity correlations for WO_x/ZrO_2 have been explored by a number of research groups [8–11]. However, these materials have rarely been investigated for fatty acid esterification, and there have been no efforts to systematically elucidate structure–reactivity relations for this class of reaction pertinent to the pre-processing of plant and aquatic bio-oils for the subsequent base catalysed transesterification of their triglyceride components to biodiesel. Heterogeneous catalysts are attractive for such esterifications since such solid acids can be readily separated from the reaction mixture by filtration, and facilitate the use of continuously operated reactors such as fixed bed and oscillatory baffled reactors [2,12–14]. The products of fatty acid esterification with light alcohols, methyl and ethyl esters can also be used directly as biodiesel, which if derived from non-edible plants, algae or waste cooking oils, is considered as a sustainable drop-in fuel for blending/substituting petroleum-derived diesel [15].

Previous studies have demonstrated that tungsten deposition onto ZrO_2 results in the genesis of strong acid sites, and it has been speculated that catalytic activity is associated with interconnected polyoxotungstate species on the zirconia surface formed at high tungsten coverages [9–11,16,17]. At near saturation monolayer coverages, W is believed to inhibit sintering of tetragonal ZrO_2 and stabilise this metastable support phase with respect to monoclinic ZrO_2 [11]. The literature consensus is that maximal catalytic activities obtain at intermediate surface tungsten densities (expressed in W atoms nm^{-2}): for n-butane isomerisation maximum activity occurred ~6 W atoms nm^{-2} [16]; for o-xylene isomerisation ~7–8 W nm^{-2} [18]; and for the trans-esterification of triacetin and acetic acid esterification ~5–6 W atoms nm^{-2} [19]. Tungstated zirconias have been subject to

various characterisations and reactivity screening to describe the surface W density, oxidation state, local W coordination, and Brönsted versus Lewis nature of acid sites [11,16,20–23]. However, absolute composition, structural properties and reactivity differ widely between studies depending on method of catalyst preparation and activation, analytical method employed and reaction operating conditions, suggesting a rich and complex character to W species dispersed over zirconia supports. The catalytic activity of WO_x/ZrO_2 has likewise not been systematically explored for fatty acid esterification, hence the present work seeks to improve our fundamental understanding of structure–acidity relations and the concomitant catalytic activity of WO_x/ZrO_2 solid acids in the low temperature esterification of palmitic acid with methanol for application in biodiesel production.

2. Experimental

2.1. Catalyst preparation

A series of WO_x/ZrO_2 catalysts were prepared by incipient-wetness impregnation of zirconium hydroxide (MelChem XZO 880/01) with aqueous solutions of ammonium (para)tungstate hydrate $((NH_4)_{10}H_2(W_2O_7)_6 \cdot xH_2O$, Sigma–Aldrich 99.99%) to yield nominal W loadings of 6.8, 15, 30 and 60 wt%. The resulting slurry was stirred for 15 h, and evaporated to dryness at 80 °C, and subsequently calcined in air at temperatures between 500 and 800 °C for 4 h. The resulting powdered solids were designated xWZr, where x is the nominal bulk W loading. Materials were benchmarked against commercial tungstated zirconium hydroxide (XZO 1251/02 Mel Chemicals) designated WZr-MelChem.

2.2. Catalyst characterisation

Nitrogen physisorption measurements were undertaken on a Quantachrome Nova 1200 porosimeter, with samples degassed at 120 °C for 2 h prior to recording adsorption/desorption isotherms. Multipoint Brunauer–Emmett–Teller (BET) surface areas were determined, with mean pore diameters calculated by applying the Barrett–Joyner–Halenda (BJH) method to the desorption isotherm. Power X-ray diffraction patterns (XRD) were collected on a PANalytical X'pertPro diffractometer fitted with an X'celerator detector and Cu K_α (1.54 Å) source. Scanning electron microscopy and energy dispersive X-ray elemental analysis (SEM/EDX) was performed on a Carl Zeiss Evo-40 instrument, with samples mounted on conductive carbon tape. X-ray photoelectron spectroscopy (XPS) was performed on a Kratos Axis HSi instrument fitted with a charge neutraliser and magnetic focusing lens employing Al K_α monochromated radiation (1486.7 eV). High resolution spectral fitting was undertaken on Shirley background subtracted data using CasaXPS version 2.3.14, with binding energies corrected to the C 1s peak at 284.5 eV a common Gaussian/Lorentzian peak shape. Surface compositions were derived applying the appropriate instrument response factors. Brönsted/Lewis acid character was determined via Diffuse Reflectance Infrared Fourier Transform Spectroscopy (DRIFTS) on a Nicolet Nexus 479 FTIR spectrometer via pyridine adsorption; approximately 1 mL of pyridine (Aldrich 99.8%) was dropped onto 200 mg of sample and dried by vacuum oven to remove physisorbed base. Acid site densities were measured on a Quantachrome CHEMBET-3000 instrument by pulse chemisorption using pure NH_3 (BOC 99.98%). Catalyst powders were degassed at 150 °C for 2 h under flowing He, with NH_3 adsorption subsequently performed at 100 °C to prevent NH_3 physisorption; titration was performed by injecting 1 mL NH_3 pulses with a gas syringe until the TCD and mass

spectrometer detector signals reached plateau. Temperature programmed desorption (NH_3-TPD) was then utilised to confirm the acid site density and evaluate acid strength; ammonia desorption was carried out between 100 and 750 °C with a heating rate of 10 °C min^{-1}.

2.3. Catalytic activity

Palmitic acid esterification reaction was performed under stirred batch conditions at atmospheric pressure in a Radley's Carousel reaction station using 25 ml glass tubes. Reactions were conducted using 10 mmol palmitic acid in 12.5 mL of methanol (molar ratio nMeOH/$n$acid = 30) at 60 °C, conditions under which the acid and methanol were fully miscible, in the presence of 50 mg catalyst and 0.59 mL of dihexylether as an internal standard. Reaction profiles were obtained via periodic sampling and analysis using a Varian 450-GC equipped with on-column injector and Phenomenex ZB-1HT Inferno wide bore capillary column (15 m × 0.53 mm × 0.15 μm). Dichloromethane was used to dilute samples for GC analysis. Catalytic profiles were an average of two separate runs, with each analysis point performed in triplicate. Turnover frequencies (TOFs) were determined from the linear portion of the initial reaction rate profile, normalised to the surface acid site density determined from ammonia pulse chemisorption and TPD.

3. Results and discussion

3.1. Catalyst characterisation

The evolution of the bulk physical properties of WO_x/ZrO_2 materials as a function of tungsten loading and calcination temperature is summarised in Table 1. For a constant calcination temperature the most pronounced changes occur at further addition than 15 wt% of the tungsten species. For the 500 and 700 °C increasing the W loading initially increased the BET surface area up to a maximum for the 15WZr sample, it can be attributed to ZrO_2 stabilisation by dispersed W species, before falling significantly for loadings above 20 wt% W. For 600 °C the surface area increase up to 19WZr sample and 800 °C the surface area decrease with increasing W loading. These non-linear results appear to be more dependent on how and which tungsten species are dispersed on the zirconia surface. In contrast, increasing the calcination temperature for constant W loading led to a continuous decrease in BET surface area. This may reflect sintering, crystallisation, and attendant pore collapse of the initial amorphous zirconia hydroxide support and/or permeation of tungsten (oxides) into the support and concomitant pore blockage [11,24]. The total pore volume and mean pore diameter are also strongly dependent upon calcination temperature: for the samples calcined at 500 and 600 °C the pore diameter is very similar for all samples and the pore volume decrease rapidly with W loading; However for samples calcined at 700 and 800 °C the pore volume only exhibits a significant decrease for W loadings >20 wt%, while the pore diameter actually increases at the highest W loading. The latter scenario is indicative of loss of support microporosity via tungstate species resulting in a smaller number of larger pores. BJH analysis of the pore size distribution on the adsorption isotherm reveals a narrow pore size distribution for the samples calcined at 500 and 600 °C and for the samples calcined at 700 and 800 °C the pore size distribution becomes larger, indicating the loss of the support porosity, probability due to permeation of tungsten (oxides) into the support and concomitant pore blockage (Figure S1, supplementary data) [17].

Supplementary Fig. S1 related to this article can be found, in the online version, at http://dx.doi.org/10.1016/j.apcatb.2014.06.036.

Table 1
Physical properties for the WO_x/ZrO_2.

Solid	Calcination temperature (°C)	Surface W content (wt%)	Surface area (m²/g)	Pore size (nm)	Pore volume (cm³/g)
12WZr		12.6	151	3.45	0.20
15WZr	500	15.3	214	3.34	0.13
19WZr		19.7	203	3.35	0.10
22WZr		22.5	160	3.35	0.09
12WZr		12.6	136	4.31	0.34
15WZr	600	15.3	131	3.42	0.25
19WZr		19.7	159	3.45	0.16
22WZr		22.5	111	3.43	0.11
12WZr		12.6	87	4.45	0.17
15WZr	700	15.3	125	3.91	0.26
19WZr		19.7	63	5.11	0.28
22WZr		22.5	48	9.91	0.13
12WZr		12.6	58	6.79	0.17
15WZr	800	15.3	56	6.72	0.16
19WZr		19.7	48	6.76	0.16
22WZr		22.5	32	10.03	0.12

The effect of calcination temperature and tungsten content on the stability of tetragonal ZrO_2 is apparent from XRD (Fig. 1). Pure ZrO_2 exhibits reflections characteristic of monoclinic ($2\theta = 28.2°$ and $31.4°$) phases as that is the thermodynamically stable phase [11,25].

In contrast, diffraction patterns for all WO_x/ZrO_2 materials were consistent with previous reports [11,19], wherein the monoclinic phase is suppressed by increasing the W loading for any given calcination temperature, evidencing stabilisation of tetragonal zirconia (t-ZrO_2). The observation of crystalline WO_3 ($2\theta = 23.1°$, $23.59°$ and $24.38°$) which is indicative of WO_x multilayer formation [9,19],

was a strong function of loading and calcination temperature; for the 500 °C calcined sample it could only be detected at the highest W loading, being more readily apparent at lower loadings as the calcination temperature rose. At lower 500 °C and 600 °C calcination temperatures the catalyst comprised primarily t-ZrO_2 and amorphous tungstate. The amount of the tetragonal and monoclinic phase was estimated by comparing the areas of the characteristic peaks of the monoclinic at 28.2° corresponding to ($1\,1\,\bar{1}$) diffraction plane and 31.4° corresponding to ($1\,1\,1$) diffraction plane and for the tetragonal peaks at 30.1° ($1\,0\,1$), 35.3° ($0\,0\,2$) and 49.8° ($1\,1\,2$). The percent composition of each phase was calculated from the
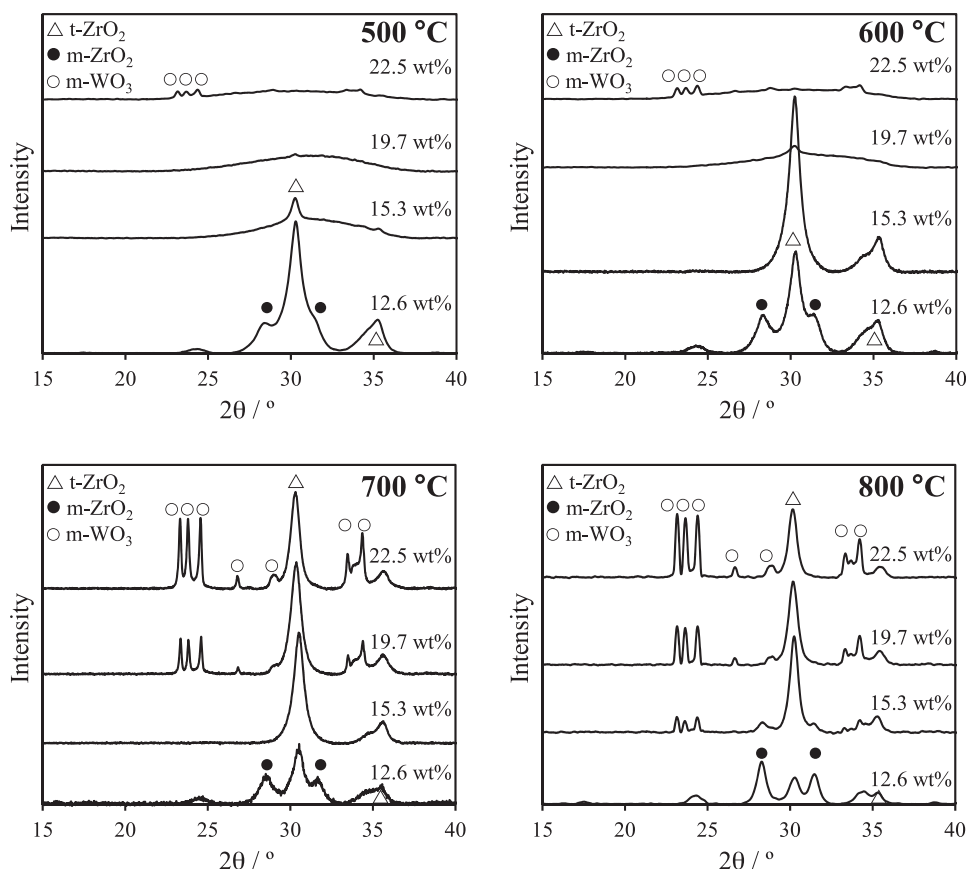

Fig. 1. Powder X-ray diffraction patterns for WO_x/ZrO_2 as a function of W loading and calcination temperature.
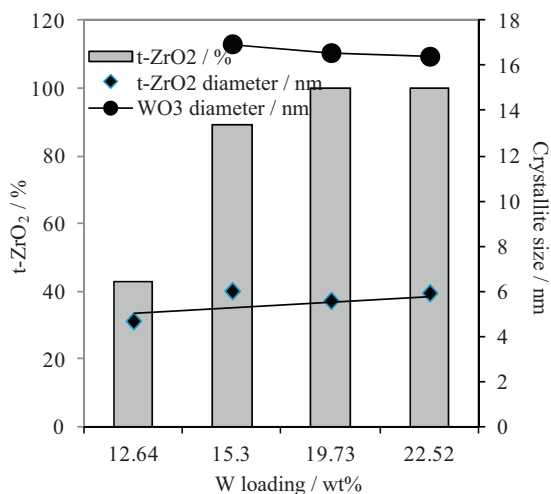
Fig. 2. Influence of W loading on proportion of tetragonal ZrO_2 and crystallite sizes for tetragonal ZrO_2 and WO_3 for WO_x/ZrO_2 materials calcined at 800 °C.

Gaussian area $h \times w$ (where h is the height and w is the half-width of the corresponding XRD peaks) as follows [26]:

$$\%Monoclinic = \frac{\sum(h \times w)monoclinic}{\sum(h \times w)tetragonal\ and\ monoclinic}$$

$$\%Tetragonal = \frac{\sum(h \times w)tetragonal}{\sum(h \times w)tetragonal\ and\ monoclinic}$$

The Gaussian area ($h \times w$) for the peaks 28.2°, 30.1°, 31.4° and 35.3° was obtained following a profile fitting procedure in order to get a decomposition of the peaks overlapped. These results are shown in Fig. 2 alongside crystallite sizes (estimated from the Scherrer equation [26]) for t-ZrO_2 and WO_3 as a function of W loading for 800 °C calcined samples. The proportion of t-ZrO_2 increased significantly with W loading above 15.3 wt%, beyond which only the tetragonal phase is present as 6 nm crystallites, however higher loadings simply increased the number of such t-ZrO_2 crystallites rather than their dimensions. The WO_3 crystallite size is significantly larger at around 16 nm and essentially loading invariant at this high processing temperature.

Thermal treatment of the 15WZr sample induced crystallisation of amorphous zirconia as both tetragonal and monoclinic zirconia, the former dominating even at 800 °C, in parallel with WO_3 crystallisation. These phase transitions, and the coincident sintering of t-ZrO_2 crystallites between 600 and 800 °C, resulted in a steep loss of surface area as shown in Fig. 3.

In order to provide a more quantitative measure of tungsten coverage, the W surface density (atoms nm^{-2}) was calculated in accordance to the literature [24,27] using the following equation:

$$W\ surface\ density = \frac{(Tungsten\ loading/100) \times N_A}{Formula\ weight\ of\ promotor \times BET\ surface\ area \times 1 \times 10^{18}}$$

The evolution of surface density with tungsten loading and calcination temperature is summarised in Fig. 4. It is evident that surface density increases non-linearly with W loading for all calcination temperatures, reflecting the loss in support surface area associated with zirconia and WO_3 crystallisation >15 wt% [11], consistent with previous reports [9,11,19]. For any given tungsten loading, higher calcination temperatures likewise increase the tungsten surface density due to the associated change in support textural properties and tungstate crystallisation.

XPS was also employed to directly quantify the tungsten surface concentration, oxidation state and growth mode. Fig. 5a and b
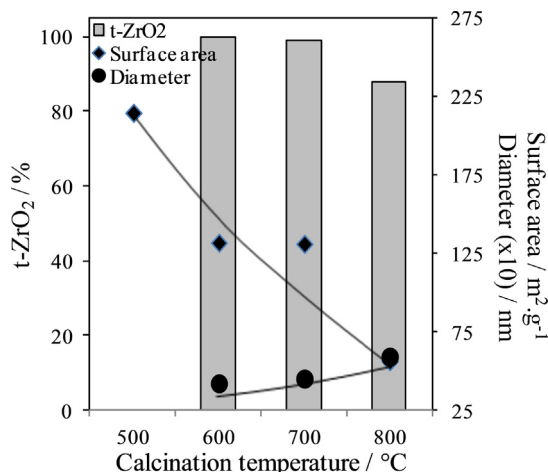

Fig. 3. Influence of calcination temperature on the proportion of t-ZrO_2 and associated crystallite size and surface area for 15WZr.
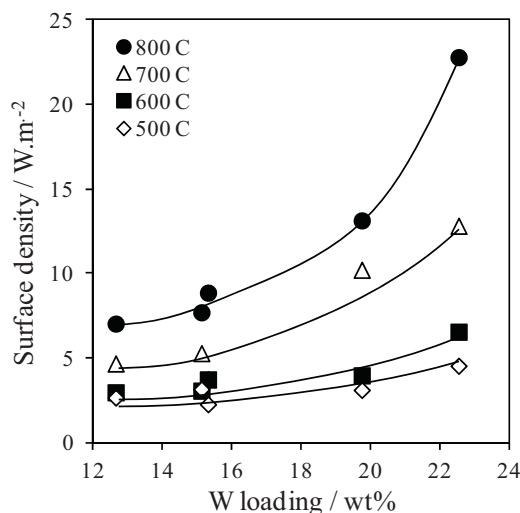

Fig. 4. Evolution of surface density with tungsten content as a function of calcination temperature for WO_x/ZrO_2 materials.

shows the evolution of W 4f and Zr 4p XP spectra as a function of W loading (following calcination at 800 °C), and calcination temperature for the 15WZr sample. In all cases, the W $4f_{7/2}$ binding energy of around 35.6 eV was characteristic of W(VI) consistent with the presence of WO_3 in agreement with XRD [28,29]. Furthermore, it can also be observed the Zr $4p_{1/2}$ binding energy around 31.82 eV, besides the Zr $3d_{5/2}$ binding energy around 182.5 eV, both signals characteristics of Zr(IV) from ZrO_2 [9]. Insight into the tungstate growth mode for the 800 °C calcined sample was derived from the W $4f_{7/2}$:Zr $3d_{5/2}$ XP ratio intensity, shown as a function of tungsten surface density in Fig. 6 [11,28,30]. This increases linearly up to ~9 W nm^{-2}, in good agreement with the theoretical density of a polytungstate monolayer on ZrO_2 (7 W nm^{-2}) [16]. Increasing the calcination temperature of the ZrW15 sample shifted the W 4f peaks to higher binding energy, likely associated with the transition from isolated WO_x species to polytungstate clusters. The formation of Zr–WO_x clusters on a ZrO_2 support have been identified from Raman spectroscopy [11] and recently by HAADF-STEM imaging in which they are proposed to influence methanol dehydration [20,21].
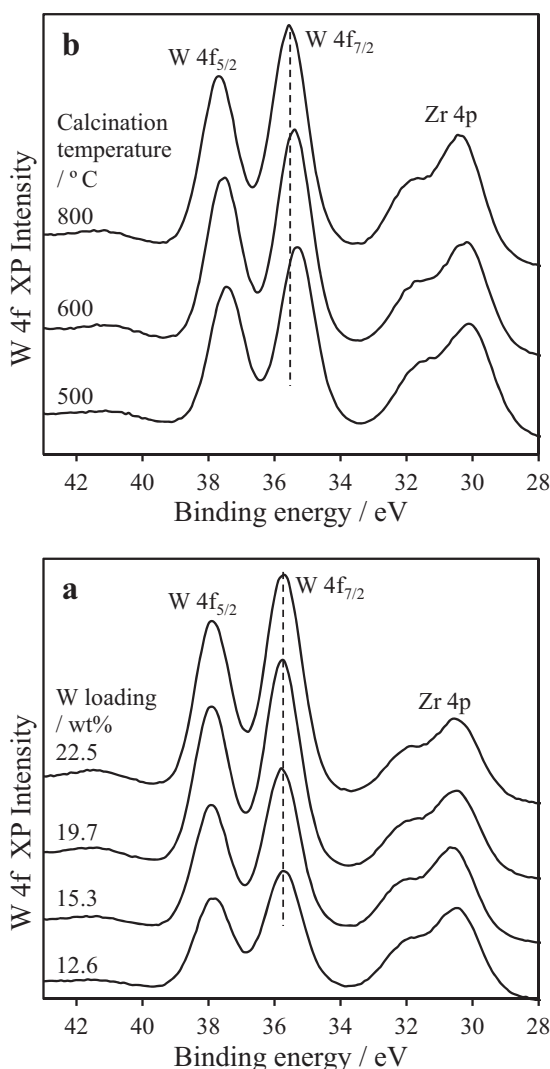
Fig. 5. W 4f and Zr 4p XP spectra of WO_x/ZrO_2 materials as a function of (a) W loading after 800 °C calcination, and (b) calcination temperature for the 15WZr sample.
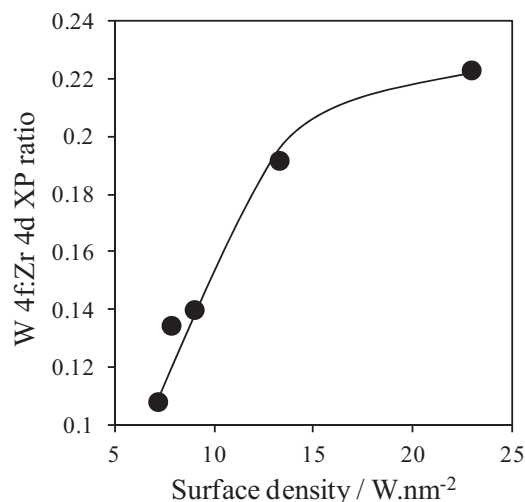

Fig. 6. Growth of surface tungstate over zirconia evidenced by W 4f:Zr 3d XP intensity ratio as a function of tungsten surface concentration for WO_x/ZrO_2 materials calcined at 800 °C.

The growth mode of tungstate species over zirconia has previously been studied in depth by Iglesia et al. [16] who identified three distinct moieties as a function of surface tungsten density utilising Raman, UV–vis, and X-ray absorption spectroscopies: isolated monotungstates species 4 W nm^{-2}; the formation of polytungstates between 4 and 8 W nm^{-2}; and crystalline WO_3 co-existing with polytungstates species upon saturation of the monolayer (>8 W nm^{-2}). In the present work, we therefore propose that at low W loadings (12.6 wt%) the dominant tungsten

species are amorphous polytungstates dispersed over a mixture of monoclinic and tetragonal zirconia. Increasing the W loading up to 15.3 wt% appears to saturate the tungstate monolayer, resulting in the appearance of large (~16 nm) WO_3 crystallites by XRD dispersed over predominantly over tetragonal zirconia (Scheme 1). Higher loadings simply increase the proportion of tungsten incorporated into this crystalline WO_3 phase. This observation presumably reflects the greater ease with which isolated monotungstate and polytungstate clusters, the precursors for crystallisation, can nucleate with decreasing separation (increasing surface density as the calcination temperature decrease the surface area of the zirconia support) via bridging W—O—W bonds between neighbouring WO_x groups to form two-dimensional polytungstates and three dimensional WO_3 crystallites.

UV–vis diffuse reflectance absorption spectra of catalysts containing different W loading and calcined at 800 °C (Fig. 7A and B) corroborates to support this proposal. The bands observed are due to the ligand to metal charge transfer (O 2p–W 5d), the energy required for this transition depends strongly of W loading and also the calcination temperature. The band at 220 nm refers to tetrahedral W(VI), at 260 nm refers to octahedral W(VI) and 350 nm refers to crystallines WO_3 species responsible of these absorptions as are showed in Fig. 7A for the WO_x standard compounds. For the samples calcined at 800 °C (Fig. 7B) those bands could be assigned to the formation of two-dimensional polytungstate on zirconia by W—O—W bonds between well dispersed $(WO)_x$ species. These extended domains of W—O—W leads to a narrowing of the HOMO–LUMO gap [16].
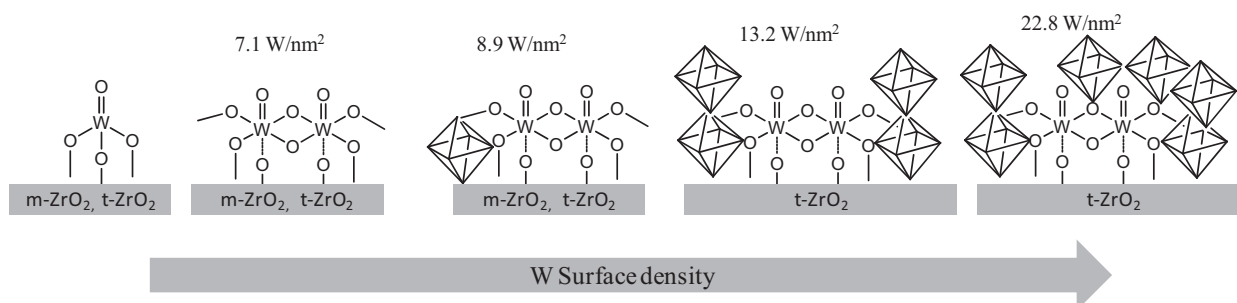
Scheme 1. Proposed growth mode of tungstates over zirconia for WO_x/ZrO_2 materials calcined at 800 °C.
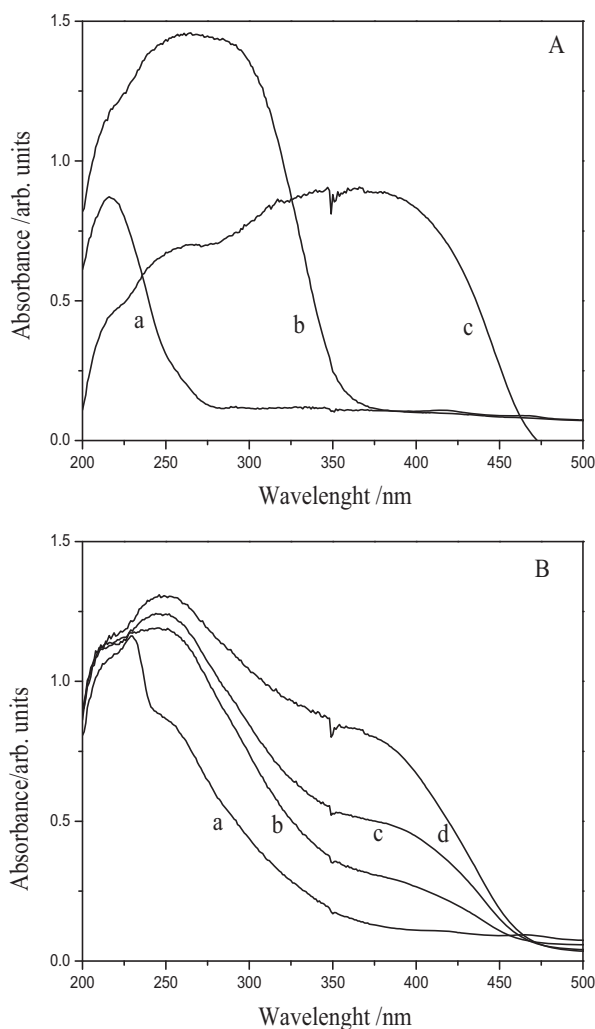
Fig. 8. Temperature-programmed desorption spectra of a saturation NH_3 adlayer from WO_x/ZrO_2 materials.

Fig. 7. Diffuse reflectance UV–vis absorption spectra for the tungsten standards A: (a) Na_2WO_4; (b) $(NH_4)_{10}H_2(W_2O_7)_6 \cdot xH_2O$ and (c) WO_3. B: WO_x/ZrO_2 materials calcined at 800 °C as a function of tungsten loading (a) 12.6 wt%, (b) 15.3 wt%, (c) 19.7 wt% and (d) 22.5 wt%.

3.2. Acid properties

The acid properties of WO_x/ZrO_2 were evaluated via NH_3-TPD analysis in order to quantify the acid site distribution in Table 2. Ammonia desorbed in a single broad feature between 150 and 600 °C for all WO_x/ZrO_2 materials, indicative of a broad range of sites with varying acid strength, illustrated for the 15WZr sample in Fig. 8. Since the desorption peak shape was independent of calcination temperature, we infer a similar distribution of weak, medium and strong acid sites, however the acid site density increased significantly following 800 °C calcination (Fig. 9a). The loading dependence for WO_x/ZrO_2 materials calcined at this high temperature was more complex (Fig. 9b), revealing a maximum for the 15WZr sample (i.e. near saturation monolayer coverage [16]), presumably reflecting a balance between the tungsten surface coverage and surface area and thus accessible tungstate species, with higher loadings locking up additional tungsten as crystalline WO_3 [16].

Further insight into the nature of the surface acid sites was obtained through pyridine adsorption and subsequent DRIFTS measurements to detect and quantify their Lewis/Brönsted character. The resulting vibrational spectra for WO_x/ZrO_2 solids calcined at 500 and 800 °C are shown in Fig. 10, revealing bands at 1580, 1540,
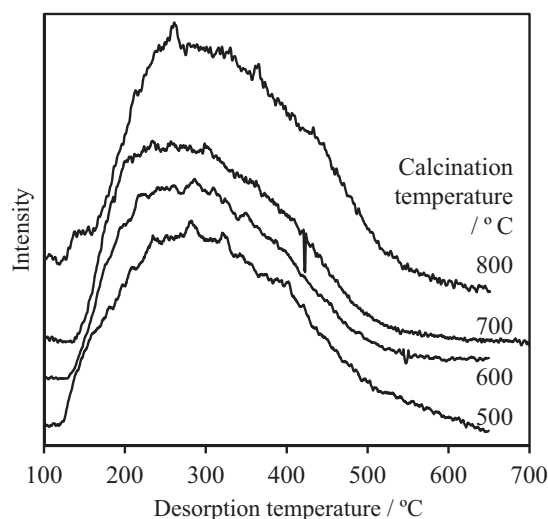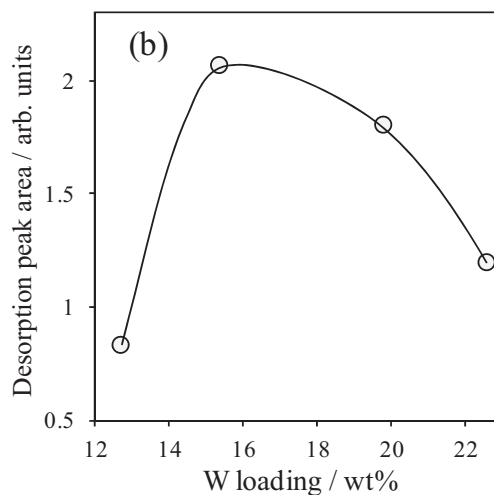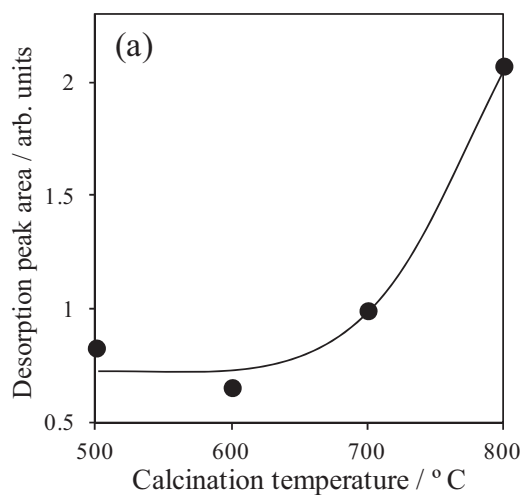

Fig. 9. Integrated NH_3 desorption peak areas of (a) 15WZr as a function of calcination temperature, and (b) WO_x/ZrO_2 materials calcined at 800 °C as a function of tungsten loading.

Table 2
Acid properties for the WO_x/ZrO_2.

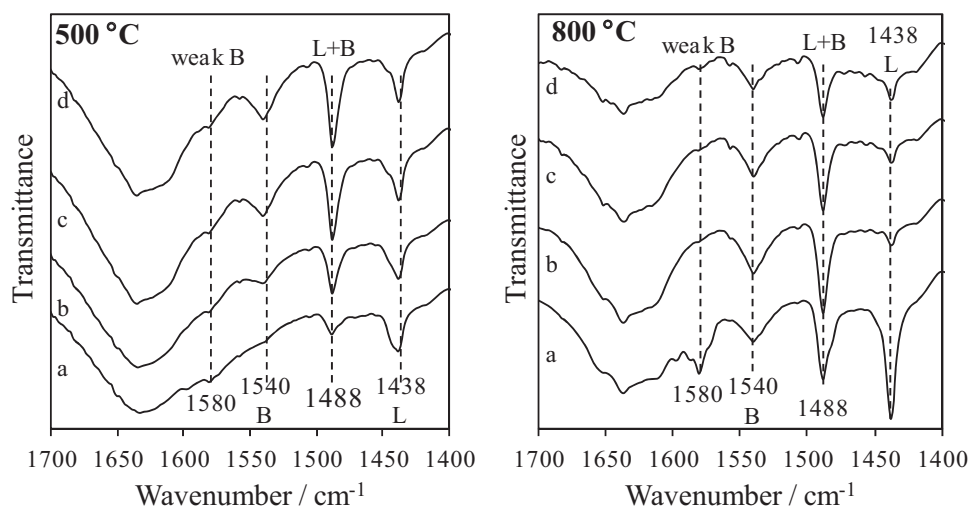| Solid	Calcination temperature (°C)	Surface W content (wt%)	Acid site loading (mmol g^{-1})[a]	Acid site density (H+ nm^2)
15WZr	500	15.3	0.295	0.828
15WZr	600	15.3	0.142	0.653
12WZr	700	12.6	0.076	0.527
15WZr		15.3	0.206	0.993
19WZr		19.7	0.075	0.717
22WZr		22.5	0.064	0.803
12WZr	800	12.6	0.081	0.837
15WZr		15.3	0.193	2.072
19WZr		19.7	0.147	1.809
22WZr		22.5	0.064	1.202

[a] Based on NH_3 desorption.

Fig. 10. DRIFT spectra of pyridine adsorbed over WO_x/ZrO_2 materials calcined at 500 °C and 800 °C as a function of tungsten loading (a) 12.6 wt%, (b) 15.3 wt%, (c) 19.7 wt% and (d) 22.5 wt%.

1488 and 1438 cm^{-1} typical of chemisorbed pyridine [17,31–34]. The band at 1540 cm^{-1} is commonly attributed to a pyridinium ion coordinated to Brönsted acid sites, with those at 1580 cm^{-1} and 1438 cm^{-1} attributed to molecular pyridine coordinated to Lewis acid sites; the 1488 cm^{-1} band is observed from pyridine adsorbed over both Brönsted and Lewis acid sites.

The relative Brönsted versus Lewis acid character can be estimated from the intensity ratio of the bands at 1540 cm^{-1} and 1438 cm^{-1} [32,33,35] and is shown in Fig. 11 for WO_x/ZrO_2 materials following low and high temperature calcination. The Brönsted:Lewis ratio for 500 °C calcined materials increases linearly with tungsten content, consistent with progressive coating of the underlying amphoteric zirconia support which possess oxygen deficient Lewis acid centres, however even the highest loading still exhibits significant Lewis acidity. Calcination at 800 °C dramatically increases the Brönsted character for all but the lowest loading (sub-monolayer) sample, for which some of the parent ZrO_2 remains exposed. However, the Brönsted:Lewis ratio exhibits a volcano dependence on loading, reaching a maximum at 15.3 wt% W, coincident with the formation of polytungstate clusters at W coverage >7 W nm^{-2}. Previous X-ray absorption studies have shown that intermediate W surface densities (4–8 W nm^{-2}) result in electron delocalisation over WO_x neighbours via the bridging W—O—W bonds present within two-dimensional polytungstate and small $(WO_3)_n$ clusters [16,30], which require charge compensation by
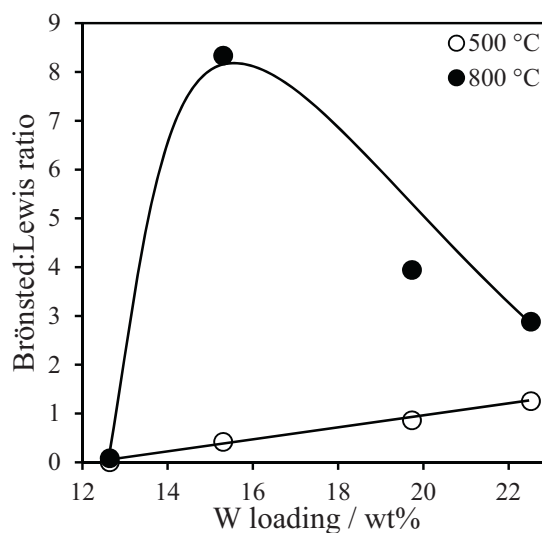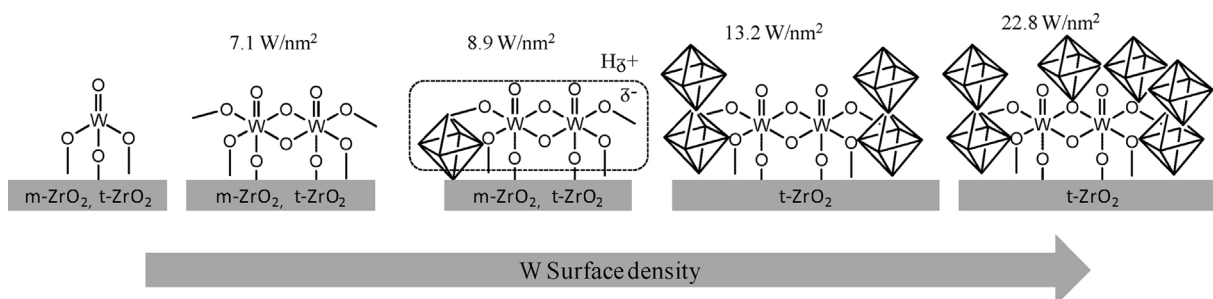

Fig. 11. Brönsted:Lewis ratio of WO_x/ZrO_2 materials determined from the DRIFT spectra of adsorbed pyridine as a function of tungsten loading.

Scheme 2. Proposed of Brönsted acid sites result by charge compensation by protons due to electron delocalisation over WO_x neighbours via the bridging W—O—W bonds tungstates over zirconia for WO_x/ZrO_2 materials calcined at 800 °C.

protons (Scheme 2). Iglesia et al. noted that <4 W nm^{-2}, zirconia stabilises electronically isolated and neutral/weakly-acidic W species. It has been suggested that the tungsten surface phase in WO_x/ZrO_2 may be viewed as pseudo-heteropolyanions of Zr-containing polytungstates, in which surface Zr^{4+} behave as lacunary substituents replacing W^{6+} ions, requiring charge compensation [18,34,36] and the concomitant formation of Brønsted acid sites. Higher tungsten loading/surface coverage promotes the phase transition to neutral WO_3 crystallites and concomitant loss of surface area.

3.3. Palmitic acid esterification

The catalytic performance of WO_x/ZrO_2 was assessed as a function of W loading and calcination temperature towards palmitic acid esterification with methanol under mild conditions (Fig. 12). In all cases, palmitic acid conversion increased with calcination

temperature, consistent with the enhanced acid site density and Brönsted acidity, with the 800 °C calcined 15WZr catalyst exhibiting the highest activity, and significantly outperforming a commercial analogue.

The catalytic performance of 800 °C calcined WO_x/ZrO_2 materials (in terms of both initial rate and turnover frequency normalised per tungsten site) for palmitic acid esterification with methanol exhibited a volcano dependence upon W surface density as shown in Fig. 13, with a maximum around 9 W nm^{-2}; this coincides with the maximum Brönsted:Lewis acid site ratio, confirming that esterification follows a Brönsted acid catalysed pathway. López et al. also reported an optimum calcination temperature of 800 °C, and slightly lower tungsten surface density of 5–6 W nm^{-2} for acetic acid esterification and triacetin transesterification with methanol, associated with surfaces containing highly dispersed WO_x species or tungstate monolayers [19]; crystalline WO_3 formed at higher W
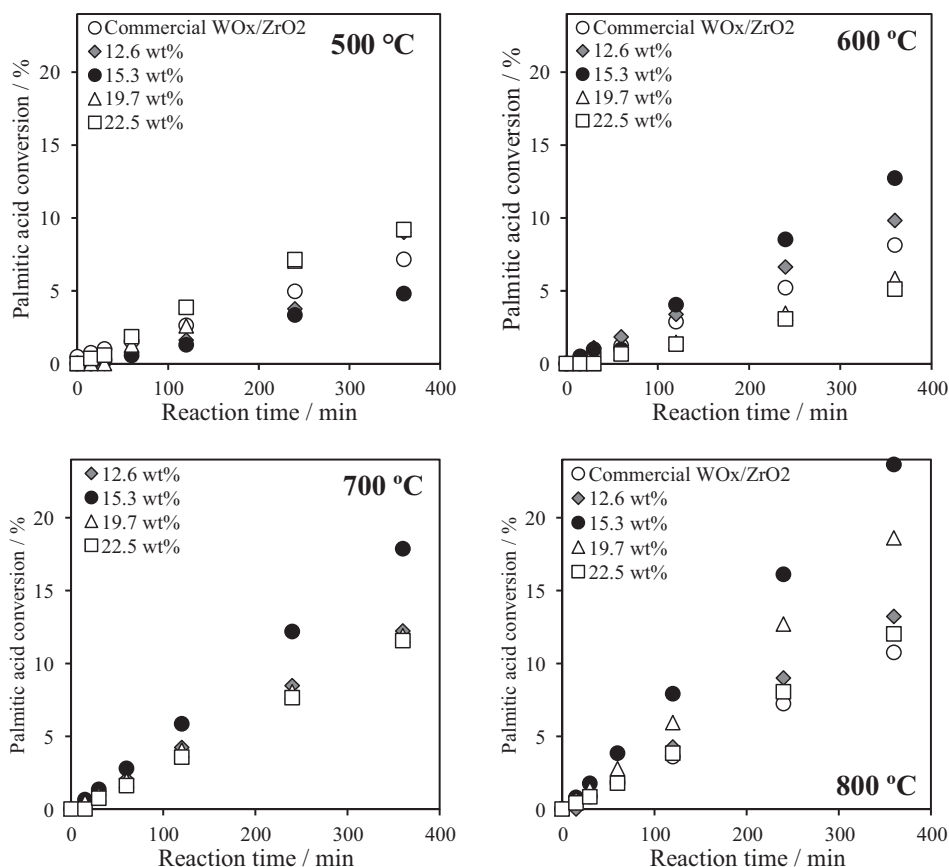

Fig. 12. Reaction profiles for palmitic acid esterification with methanol over WO_x/ZrO_2 catalysts as a function of calcination temperature and tungsten loading. Conditions: 60 °C, 12.5 mL MeOH, 30:1 molar ratio MeOH:palmitic acid.
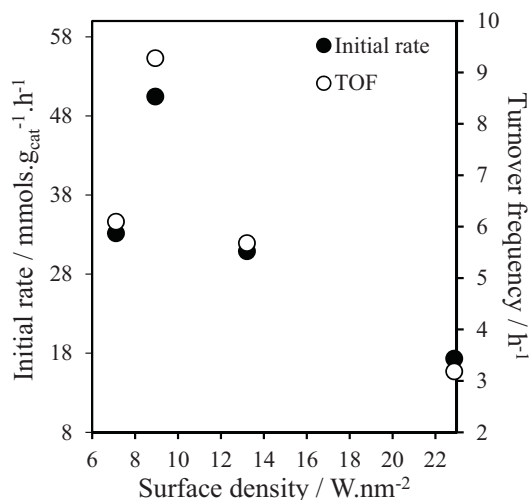
Fig. 13. Dependence of initial rate and turnover frequency per tungsten for palmitic acid esterification over 800 °C calcined WO_x/ZrO_2 catalysts as a function of surface tungsten density. Conditions: 60 °C, 12.5 mL MeOH, 30:1 molar ratio MeOH:palmitic acid.

Fig. 15. Impact of solvothermal reaction conditions upon palmitic acid esterification over 800 °C calcined 15 wt% WO_x/ZrO_2. Conventional conditions: 60 °C, 12.5 mL MeOH, 30:1 molar ratio MeOH:palmitic acid; solvothermal conditions: 120 °C, 12:1 molar ratio MeOH:palmitic acid and 10 wt% catalyst.

loadings proved less active for methyl ester production in accordance with the present work. Ramu et al. [37] likewise reported a volcano dependence of palmitic acid esterification upon tungsten loading, noting optimal performance at a significantly lower W loading (~5 wt%) and calcination temperature (500 °C). Turnover frequencies normalised per proton were comparable to literature values for higher surface area, mesoporous sulfonic acid silicas under similar reaction conditions [4,38,39], with the optimum 15WZr sample exhibiting a TOF of 40 h^{-1} after 800 °C calcination.

Catalyst stability and reusability was examined for the most active 15 wt% WO_x/ZrO_2 material calcined at 800 °C (Fig. 14). The spent catalyst was recovered via filtration, washed in methanol, and subsequently re-used for two further esterifications runs employing a fresh reaction mixture each time either with or without re-calcination at 800 °C between each recyle. Little deactivation was observed for either scenario after only one reaction, however the uncalcined sample showed significant loss in activity upon the second recycle, suggesting catalyst deactivation occurred via carbon lay down or an in-situ (and thermally reversible) phase transition of surface tungstate or zirconia support. Finally, the impact of
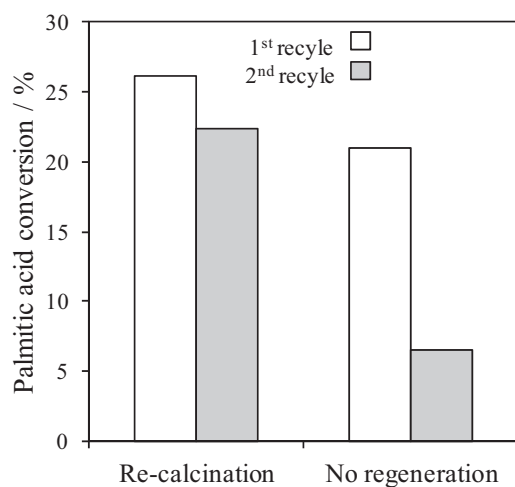
solvothermal reaction conditions was assessed via high temperature (120 °C) palmitic acid esterification within a stirred autoclave, which revealed a dramatic increase in conversion relative to the conventional conditions (Fig. 15).

4. Conclusion

The influence of W loading and calcination temperature was investigated upon the catalytic activity of WO_x/ZrO_2 towards the esterification of palmitic acid with methanol. High temperature calcination was necessary to induce crystallisation of tetragonal zirconia, coalescence of isolated WO_x clusters as polytungstates and the genesis of Brönsted acid sites. Highest activity was observed for catalysts comprising 15.3 wt% tungsten, corresponding to a surface density of 8.9 W nm^{-2}, close to the theoretical, saturation monolayer coverage of 7 W nm^{-2}; higher surface W densities promoted the formation of inert WO_3 crystallites. Polymeric tungsten species supported on tetragonal zirconia appear critical to create the requisite Brönsted acid sites for palmitic acid esterification. The optimum 15 wt% WO_x/ZrO_2 catalyst was resistant to leaching, and could be readily recovered and recycled without major activity loss employing simple thermal regeneration. Zirconia hydroxide thus appears an excellent, low cost support for stabilising catalytically active acidic tungstate species for fatty acid esterification.

Fig. 14. Regeneration of spent 15 wt% WO_x/ZrO_2 for palmitic acid esterification via 800 °C re-calcination. Conditions: 60 °C, 12.5 mL MeOH, 30:1 molar ratio MeOH:palmitic acid.
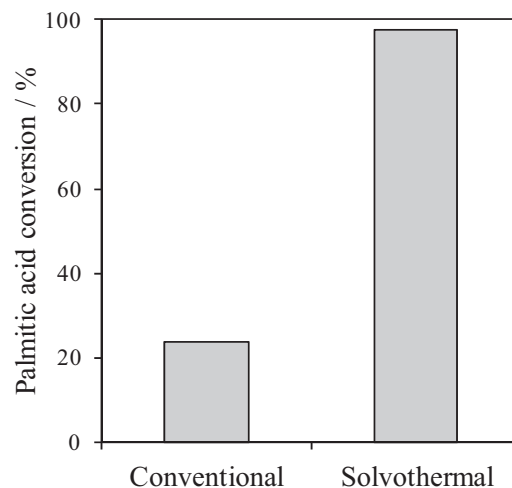
References

[1] J. Hagen, Industrial Catalysis A Practical Approach, Wiley-VCH, 1999.
[2] K. Wilson, A.F. Lee, Catal. Sci. Technol. 2 (2012) 884–897.
[3] J.L.G. Fierro, Metal Oxides: Chemistry and Applications, Taylor & Francis Group, 2006.
[4] J. Dhainaut, J. Dacquin, A.F. Lee, K. Wilson, Green Chem. 12 (2010) 296–303.
[5] M. Hino, K. Arata, J. Chem. Soc. Chem. Commun. (1987) 1259.
[6] G.D. Yadav, J.J. Nair, Microporous Macroporous Mater. 33 (1999) 1–48.
[7] M.Y. Smirnova, A.V. Toktarev, A.B. Ayupov, G.V. Echevsky, Catal. Today 152 (2010) 17–23.

[8] N. Soultanidis, W. Zhou, A.C. Psarras, A.J. Gonzalez, E.F. Iliopoulou, C.J. Kiely, I.E. Wachs, M.S. Wong, J. Am. Chem. Soc. 132 (2010) 13462–13471.

[9] F. Di Gregorio, V. Keller, J. Catal. 225 (2004) 45–55.

[10] C.D. Baertsch, S.L. Soled, E. Iglesia, J. Phys. Chem. B 105 (2001) 1320–1330.

[11] E.I. Ross-Medgaarden, W.V. Knowles, T. Kim, M.S. Wong, W. Zhou, C.J. Kiely, I.E. Wachs, J. Catal. 256 (2008) 108–125.

[12] V.C. dos Santos, A. Bail, H.O. Okada, L.P. Ramos, K.J. Ciuffi, O.J. Lima, S. Nakagaki, Energy Fuels 25 (2011) 2794–2802.

[13] K.N. Rao, A. Sridhar, A.F. Lee, S.J. Tavener, N.A. Young, K. Wilson, Green Chem. 8 (2006) 790–797.

[14] V.C. Eze, A.N. Phan, C. Pirez, A.P. Harvey, A.F. Lee, K. Wilson, Catal. Sci. Technol. 3 (2013) 2373–2379.

[15] A. Bail, V.C. dos Santos, M.R. de Freitas, L.P. Ramos, W.H. Schreinerc, G.P. Ricci, K.J. Ciuffi, S. Nakagaki, Appl. Catal. B 130–131 (2013) 314–324.

[16] D.G. Barton, M. Shtein, R.D. Wilson, S.L. Soled, E. Iglesia, J. Phys. Chem. B 103 (1999) 630–640.

[17] A.H. Karim, S. Triwahyono, A.A. Jalil, H. Hattori, Appl. Catal. A 433–434 (2012) 49–57.

[18] D.G. Barton, S.L. Soled, E. Iglesia, Top. Catal. 6 (1998) 87–99.

[19] D.E. Lópes, K. Suwannkarn, D.A. Bruce, J.G. Goodwin Jr., J. Catal. 247 (2007) 43–50.

[20] W. Zhou, E.I. Ross-Medgaarden, W.V. Knowles, M.S. Wong, I.E. Wachs, C.J. Kiely, Nat. Chem. 1 (2009) 722–728.

[21] W. Zhou, I.E. Wachs, C.J. Kiely, Curr. Opin. Solid State Mater. Sci. 16 (2012) 10–22.

[22] M.A. Cortés-Jácome, C. Angeles-Chavez, E. López-Salinas, J. Navarrete, P. Toribio, J.A. Toledo, Appl. Catal. A 318 (2007) 178–189.

[23] M. Scheithauer, R.K. Grasselli, H. Knozinger, Langmuir 14 (1998) 3019–3029.

[24] P. Wongmaneenil, B. Jongsomjit, P. Praserthdam, Catal. Commun. 10 (2009) 1079–1084.

[25] W. Stichert, F. Schuth, Chem. Mater. 10 (1998) 2020–2026.

[26] N. Senso, B. Jongsomjit, P. Praserthdam, Fuel Process. Technol. 92 (2011) 1537–1542.

[27] S. Praserthdam, P. Wongmaneenil, B. Jongsomjit, J. Ind. Eng. Chem. 16 (2010) 935–940.

[28] M. Valigi, D. Gazzoli, I. Pettiti, G. Mattei, S. Colonna, S. De Rossi, G. Ferraris, Appl. Catal. A 231 (2002) 159–172.

[29] F.Y. Xie, L. Gong, X. Liu, Y.T. Tao, W.H. Zhang, S.H. Chen, H. Meng, J. Chen, J. Electron Spectrosc. Relat. Phenom. 185 (2012) 112–118.

[30] B.M. Devassy, S.B. Halligudi, J. Catal. 236 (2005) 313–323.

[31] N. Naito, N. Katada, M. Niwa, J. Phys. Chem. B 103 (1999) 7206–7213.

[32] R. Sakthivel, H. Prescott, E. Kemnitz, J. Mol. Catal. A: Chem. 223 (2004) 137–142.

[33] G. Sunita, B.M. Devassy, A. Vinu, D.P. Sawant, V.V. Balasubramanian, S.B. Halligudi, Catal. Commum. 9 (2008) 696–702.

[34] A. El Rahman, S. Khdera, H.M.A. Hassana, M.S. El-Shall, Appl. Catal. A 411–412 (2012) 77–86.

[35] E.P. Parry, J. Catal. 2 (1963) 371–379.

[36] R. Villanneau, H. Carabineiro, X. Carrier, R. Thouvenot, P. Herson, F. Lemos, F.R. Ribeiro, M. Che, J. Phys. Chem. B 108 (2004) 12465–12471.

[37] S. Ramu, N. Lingaiah, B.L.A. Prabhavathi Devi, R.B.N. Prasad, I. Suryanarayan, P.S. Sai Prasad, Appl. Catal. A 276 (2004) 163–168.

[38] J.P. Dacquin, A.F. Lee, C. Pirez, K. Wilson, Chem. Commun. 48 (2012) 212–214.

[39] C. Pirez, J.M. Caderon, J.P. Dacquin, A.F. Lee, K. Wilson, ACS Catal. 2 (2012) 1607–1614.